South Asian Haze Forcing: Remote Impacts with Implications to ENSO and AO

CHUL EDDY CHUNG AND V. RAMANATHAN

Center for Clouds, Chemistry and Climate, Scripps Institution of Oceanography, La Jolla, California

(Manuscript received 3 May 2002, in final form 2 December 2002)

ABSTRACT

Aerosols are regionally concentrated and are subject to large temporal variations, even on interannual timescales. In this study, the focus is on the observed large interannual variability of the South Asian (SA) haze, estimating the corresponding variations in its radiative forcing, and using a general circulation model to study their impacts on global climate variability. The SA haze is a widespread haze, covering most of South Asia and the northern Indian Ocean during December–April. The southernmost extent of the haze varies year to year from about 10°S to about 5°N. In order to understand the impact of this interannual variation in the haze forcing, two numerical studies were conducted with two extreme locations of the forcing: 1) extended haze forcing (EHF) and 2) shrunk haze forcing (SHF). The former has the forcing extending to 10°S, while the latter is confined to regions north of the equator.

Each of the two haze forcing simulations was implemented into a 3D global climate model (NCAR CCM3) with a prescribed SST seasonal cycle to estimate the sensitivity of the model climate to the aerosol forcing area. In both simulations, the haze forcing was prescribed only during the dry season between November and April. Over India where the forcing is centered, the simulated climate changes are very similar between EHF and SHF. In remote regions, however, the responses differ remarkably. Focusing on the remote effects of the haze, it is shown that some of the recent observed boreal-wintertime changes of the southwest Asian monsoon, El Niño–Southern Oscillation (ENSO), and the Arctic Oscillation (AO) could be explained by the SA haze forcing and its fluctuation.

First, both simulations reveal the wintertime drought over southwest Asia, with the EHF generating far more severe drought. Second, the EHF experiment simulates a poleward shift of the Northern Hemisphere (NH) zonal-mean zonal momentum during the winter season, while the SHF effect rather moves the NH extratropical zonal momentum only slightly equatorward. Thus, the interannual fluctuations in the extension of the haze forcing area can explain the recently documented increased variability of the AO.

Third, the EHF significantly suppresses the convection in the western equatorial Pacific during the boreal wintertime, and the SHF leads to much less suppression. Since the western Pacific convection suppression would weaken the trade winds over the Pacific and induce warm anomalies in the eastern basin, it is proposed that the SA haze may be partially responsible for the observed El Niño–like warming during the recent decades. When the convection suppression in the EHF experiment is imposed in the Cane–Zebiak Pacific ocean–atmosphere model, the coupled model actually simulates a warm bias similar to the observed El Niño trends of the recent decades. These findings have to be verified with a fully coupled ocean–atmosphere climate model.

1. Introduction

Anthropogenic climatic forcing consists primarily of greenhouse gas concentration increase, change in aerosol release, and land surface usage change. Out of these three, aerosol is the hardest problem for climate modelers because its forcing details are very uncertain. The forcing uncertainties arise partially from the fact that aerosols are short-lived in the troposphere. As a result of the short lifetimes, their spatial distributions are strongly influenced by atmospheric transport. Due to the dependence on the transport, aerosols exist very heterogeneously in space and thus form several spots (i.e., marked areas) on the earth, each of which is regionally concentrated around the sources. A strong role of the transport causes the aerosol concentrations to vary temporally on timescales ranging from minutes to months/years/decades.

One of the notable aerosol hot spots is the South Asian (SA) haze—the focus of this study. The Indian Ocean Experiment (INDOEX) documented this haze from 1995 to 2000 (Ramanathan et al. 2001, hereafter referred to as R01). This haze, about the size of the United States, extends from the south Asian continent to the Arabian Sea and from the Bay of Bengal to the Indian Ocean ITCZ. In the vertical direction, it extends from the surface to about 3 km. Roughly 75% of the particles in the haze are emitted by human activities. The brown haze phenomenon begins in December and lasts at least until the end of April. Figure 1 depicts the aerosol optical depths (AODs) of the SA haze for the months of Feb-

Corresponding author address: Chul Eddy Chung, Center for Atmospheric Sciences, Scripps Institution of Oceanography, (Mail #: 0221) 9500 Gilman Drive, La Jolla, CA 92093.
E-mail: cchung@fiji.ucsd.edu

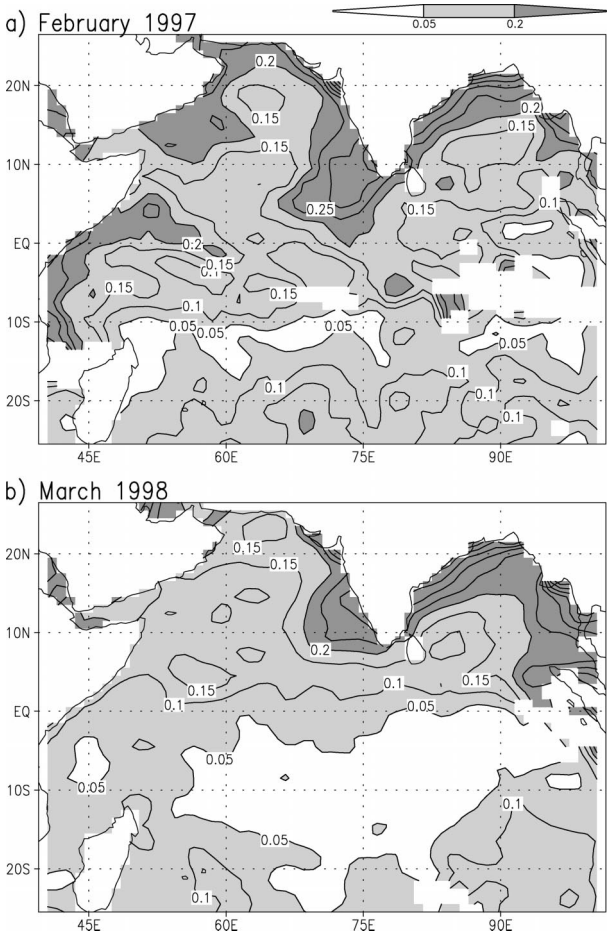

FIG. 1. Monthly mean AODs at 630 nm over the Indian Ocean for (a) Feb 1997 and (b) Mar 1998. The AODs were retrieved from the satellite AVHRR observations (as explained in Li and Ramanathan 2002). AOD is the vertical integral of aerosol concentration weighted with the effective cross-sectional area of the particles intercepting (by scattering and absorption) the solar radiation at the wavelength of interest. The higher the AOD is, the more aerosol there is.

ruary 1997 and March 1998 (obtained from Li and Ramanathan 2002). Both months had a widespread presence of the haze, and yet the southward extent varied substantially from one year to another. In February 1997, the haze reached as far as 10°S, but in March 1998 it stayed north of the equator.

The temporal variability aspect may be particularly important in the case of absorbing aerosols, since the absorption of the solar radiation by aerosols is another source of atmospheric diabatic heating (R01); scattering aerosols such as sulfate particles on the other hand exert very little direct influence on the atmospheric solar heating, and they impact the climate primarily by reducing the solar radiation reaching the surface. The SA haze is diagnosed (R01) to contain as much as about 14% black carbon by mass along with many other kinds of particle. Black carbon is the most efficient absorber among the atmospheric particulate species and, combined with dust and other aerosols, reduces the visible single scattering albedo to less than 0.9 both inland and over the open ocean. This highly absorptive aerosol layer generates an atmospheric diabatic heating of up to $+0.8$ K day^{-1} in the lower troposphere regionally (R01). This SA haze driven diabatic heating is in the same order of magnitude as a deep heating anomaly of 2 K day^{-1} during moderate ENSO events (diagnosed by Nigam et al. 2000). Atmospheric diabatic heating perturbations can impact the climate in remote regions, and furthermore such impacts might be quite different if the heating varies temporally. The Indo–Asian absorbing haze enhances the solar heating of the low atmosphere by as much as 50% $\sim$ 100% and reduces the net surface solar flux by as much as 15 $\sim$ 40 W m^{-2} (R01).

In this study, we assess the significance of the interannual variations in the aerosol forcing through two numerical sensitivity experiments with the National Center for Atmospheric Research (NCAR) Community Climate Model version 3 (CCM3): 1) extended haze forcing and 2) shrunk haze forcing. The extended haze forcing (EHF) case has the forcing extending up to 10°S, and for the shrunk haze forcing (SHF) case the forcing is restricted to the area north of the equator. These two cases represent two extreme phases of the observed AODs over the Indian Ocean (Li and Ramanathan 2002). Both numerical simulations were conducted with the climatological seasonal cycle of sea surface temperatures (SSTs). We examine the difference between the two numerical experiments to understand the sensitivity of the climate to potential variations in the aerosol forcing. This study is an initial step toward the understanding of the effects of varying aerosol distributions.

The other focus of this study is the remote impact of the aerosols. This is a particularly important issue with the SA haze since the haze creates a large atmospheric diabatic heating. R01 and Chung et al. (2002) sought to understand the regional effects of the SA haze during the northeast monsoon season using the NCAR CCM3. Expanding their works, we assess here how the regionally confined SA haze affects remote regions. In particular, our focus is on the following regions and phenomena: wintertime rainfall over southwest (SW) Asia, El Niño–Southern Oscillation (ENSO), and the Arctic Oscillation (AO). These aspects are targeted because the SA haze forcing exerts significant influences on them and the influences differ substantially between the EHF and the SHF cases. Since the EHF and the SHF depict two extreme cases of the interannual variability of the haze extent, these two sensitivity simulations by the CCM3 offer insights into the potential impacts of the haze on climate variability. When ENSO variability is addressed, we will combine the CCM3 with a tropical Pacific coupled model (designed by Zebiak and Cane 1987). We caution, however, that the present study ignores coupling with the Indian Ocean climate (since SSTs are prescribed in the CCM3) and hence is just a

first step toward an understanding of this important phenomenon.

The characteristics of recent ENSO variability have been a controversial issue. Trenberth and Hoar (1996, 1997) noted that El Niño events have been increasingly dominating over La Niña events since 1976 and suggested an anthropogenic origin for this in view of its unusualness. Correspondingly, several others (e.g., Meehl and Washington 1996) noticed a warming trend at the surface in the tropical Pacific during the recent decades, and found the trend to be projected positively onto the El Niño pattern (i.e., weakened zonal gradient of SST). Perhaps because this El Niño–like warming is accompanied by a mean warming trend, the increase in greenhouse gases has been the only anthropogenic suspect for the underlying cause.

Similarly, the discussions of the AO behavior have not included tropospheric aerosol effects either. The AO represents out-of-phase variations in the upper-level westerlies in the latitude band between about 35° and 60° (Thompson and Wallace 2000), and coincides with the ''North Atlantic Oscillation (NAO)'' or the ''Northern Hemispheric (NH) annular mode'' (Wallace 2000). During the recent decades, the AO preferred the so-called high index mode corresponding to a poleward shift of the midlatitude jet stream and main storm activity as well as a contraction of the polar vortex. This ''upward'' trend of the AO has been attributed to chaotic internal dynamics (James and James 1992), SSTs (Rodwell et al. 1999), greenhouse gases (Gillett et al. 2002), volcanic aerosols (Robock and Mao 1992), and ozone depletion (Hartmann et al. 2000). Perhaps equally important about the recent AO behavior is an increasing variance of the AO index, as just noted by Feldstein (2002). In this study, we would like to propose that the SA haze may partially explain the observed increase in the variance of the AO index as well as the observed El Niño–like warming.

This paper is organized into six sections. In section 2, the adequacy of the CCM3 as the investigation tool is first discussed. Then the details of the two sensitivity experiments are presented. This section also shows that these two experiments drive similar local changes. Section 3 describes the remote impact of the haze on wintertime precipitation over SW Asia. Remote effects of the SA haze on the tropical Pacific are discussed in section 4, where additional numerical experiments using the Cane–Zebiak model are discussed. In section 5, the analysis of the impacts on AO is presented. Discussions and conclusions follow in section 6.

2. Design of the numerical experiments

a. Adequacy of CCM3

The reliability of our results depends on the fidelity of the model in simulating the observation and on the accuracy of the imposed aerosol forcing. We refer to the *J. Climate* special issue [1998, vol. 11, no. 6; e.g., see Kiehl et al. (1998) and other papers] for a comprehensive assessment of the CCM3 performance, and the *J. Geophysical Research* INDOEX special issue (2001, vol. 106, no. D22; see R01 and other papers) for the characteristics of the SA haze and its radiative forcing. In this subsection, we focus on the precipitation climatology by the CCM3 over the relevant areas in order to gauge the adequacy of the CCM3 for the present investigation. In section 5, where the Arctic Oscillation (leading atmospheric variability) is discussed, the AO simulated by the CCM3 is compared to the corresponding observation.

Figure 2 compares the CCM3 precipitation with observed values in four geographical areas: (i) tropical India (Indian landmass south of 20°N), (ii) SW Asia (i.e., 25°–40°N, 50°–65°E in this section), (iii) the tropical Indian Ocean (10°S–10°N, 50°–100°E), and (iv) the tropical western Pacific (10°S–10°N, 10°–150°E). The simulation in Fig. 2 was obtained by forcing the CCM3 with the 1949–99 varying SST observation and then taking a mean over 1979–99. The observed climatology used in Fig. 2 is the Climate Prediction Center (CPC) Merged Analysis of Precipitation (CMAP; Xie and Arkin 1997) over 1979–99.

As Fig. 2 shows, the simulated and the observed precipitations are in good agreement during the wintertime (December–February). During this season, the difference between the CCM3 precipitation and the observation is marginal except over the tropical western Pacific where the CCM3 exceeds observations by about 15%–20%. During springtime, tropical India and the tropical western Pacific have too much precipitation in the CCM3 but the other areas do not have such substantial discrepancies. Overall, the CCM3 does relatively well from December to March—the period of focus in this study.

b. Details of the numerical experiments

Aerosols have both direct and indirect effects on the radiative heating of the earth–atmosphere system (see R01 for details). The direct effect of aerosols arises from scattering and absorption of solar radiation. Aerosols can change the climate indirectly as well, for example, by producing more cloud drops (with smaller effective radius) that in turn increases the cloud albedo. In this study, we only consider the direct effects of the SA haze in the two haze simulations (EHF and SHF).

The fundamental input for the forcing estimates is the regional distribution of the monthly mean visible ($\sim$0.55 μm) AODs reported in R01 and Li and Ramanathan (2002). We used these results to guide our selection of the two extreme cases of the haze spatial extent. We made use of the 3D aerosol heating rate estimates from the AODs that were obtained by combining the composite vertical profile of aerosol concentration (R01) with the Monte Carlo Aerosol Cloud Ra-

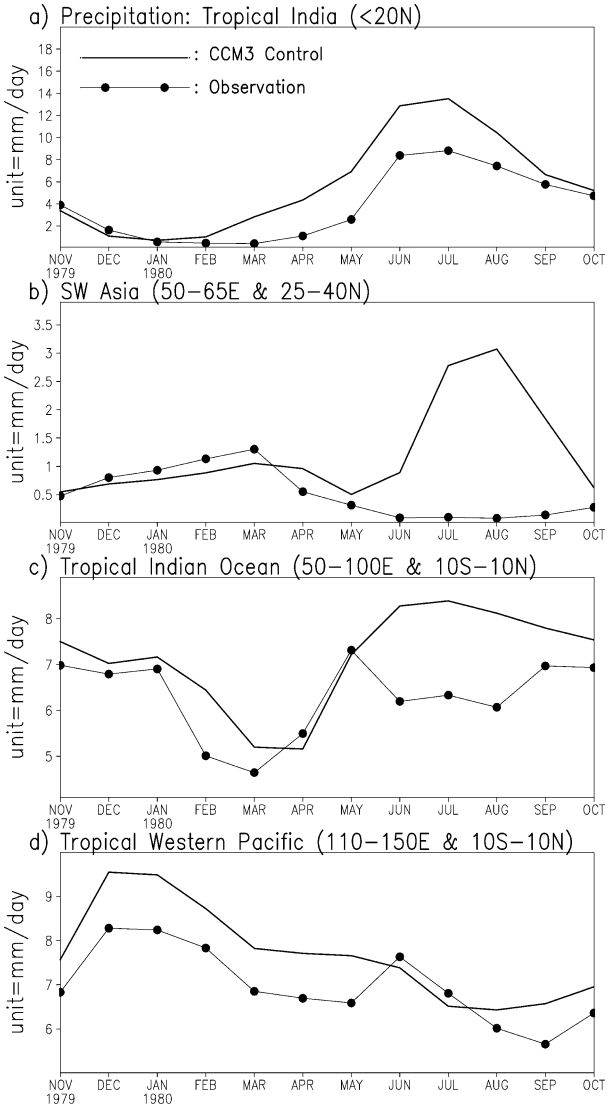

FIG. 2. The seasonal cycle of the precipitation climatology simulated with CCM3, in comparison with the observed precipitation climatology, for the purpose of gauging the model deficiencies in the areas highly relevant to the present study. The CCM3 was forced by the observed SST from 1949 to 1999 and the mean was taken over 1979–99 and over seven ensemble runs, while the observed precipitation was obtained from the 1979–99 CMAP (Xie and Arkin 1997).

diation (MACR) model described in Podgorny and Ramanathan (2001).

The EHF case has the forcing applied northward of 10°S, and the SHF is restricted to the regions north of the equator (as shown in Figs. 3a,b,d,e). Other than the spatial extent, these two experiments are identical. The haze effects were implemented into the CCM3, which was then integrated with the climatological seasonal cycle of SSTs and the interactive land surface model. The haze forcing is imposed between October and May as explained in Chung et al. (2002, see their Fig. 2). During the wet monsoon season (June–September), the model was integrated without the haze effects. The EHF experiment is identical to the "$R \cong -0.9$" case described in Chung et al. (2002), which also describes the details of the numerical experiment. Note that in these preliminary experiments various feedbacks between the haze and the atmospheric/oceanic circulation are not allowed. We conducted 60 model years of integration with the EHF effects and 45 years with the SHF effects, and contrasted each run with 85 years of the control run (i.e., run without any SA haze effects). We are concerned mainly with the mean climate change between the runs. The statistics of the mean climate were found to be insensitive to the length of the model integration provided it exceeded 40 years, and hence we interrupted the EHF case after 60 years and the SHF case after 45 years. Chung et al. (2002) have also shown that this length of CCM3 integration is sufficient for most features of the mean climate change to be statistically significant in the Tropics relative to the model internal variability. A standard *t* test supports the statistical significance for the salient features of the extratropical results as well; the significance issue will be addressed further in section 6.

Figures 3a and 3d shows the imposed solar heating rates and the computed reduction in the solar flux at the surface (Figs. 3d and 3e) for the EHF and SHF cases. As shown in this figure, the haze forcing has two opposing effects: a cooling effect at the surface and a warming effect in the lower atmosphere.

c. Local impacts versus remote impacts

The local impacts refer to the changes in the region within the domain of the imposed haze forcing. Changes outside this region are referred to as remote effects. In Figs. 3c and 3f we show the change in the velocity potential at the 200-hPa level to give an overview of the local and the remote effects. The 200-hPa level is a pressure level at which both the baroclinically responding tropical atmosphere and the barotropically responding midlatitude atmosphere produce large signals. Focusing first on Fig. 3c, the local response to the imposed solar heating is a divergent flow (negative contours as indicated by the dashed contours) within the upper troposphere. At low latitudes, diabatic heating is largely balanced by adiabatic cooling from rising motions (positive vertical velocity). The divergent flow in Fig. 3c is tied up with the vertical flow. One interesting feature is the wavenumber-1-type response, that is, the planetary-scale response to the imposed heating. A similar feature can be gleaned in Fig. 3f for the SHF, but the spatial extent and the magnitude are much smaller and weaker. As can be inferred from Figs. 3c and 3f, the EHF drives one order of magnitude bigger global impacts than the SHF as far as the mean climate change is concerned. A detailed explanation of the fundamental reason for such a nonlinear response will be addressed in a follow-up study; it appears to be related to the fact

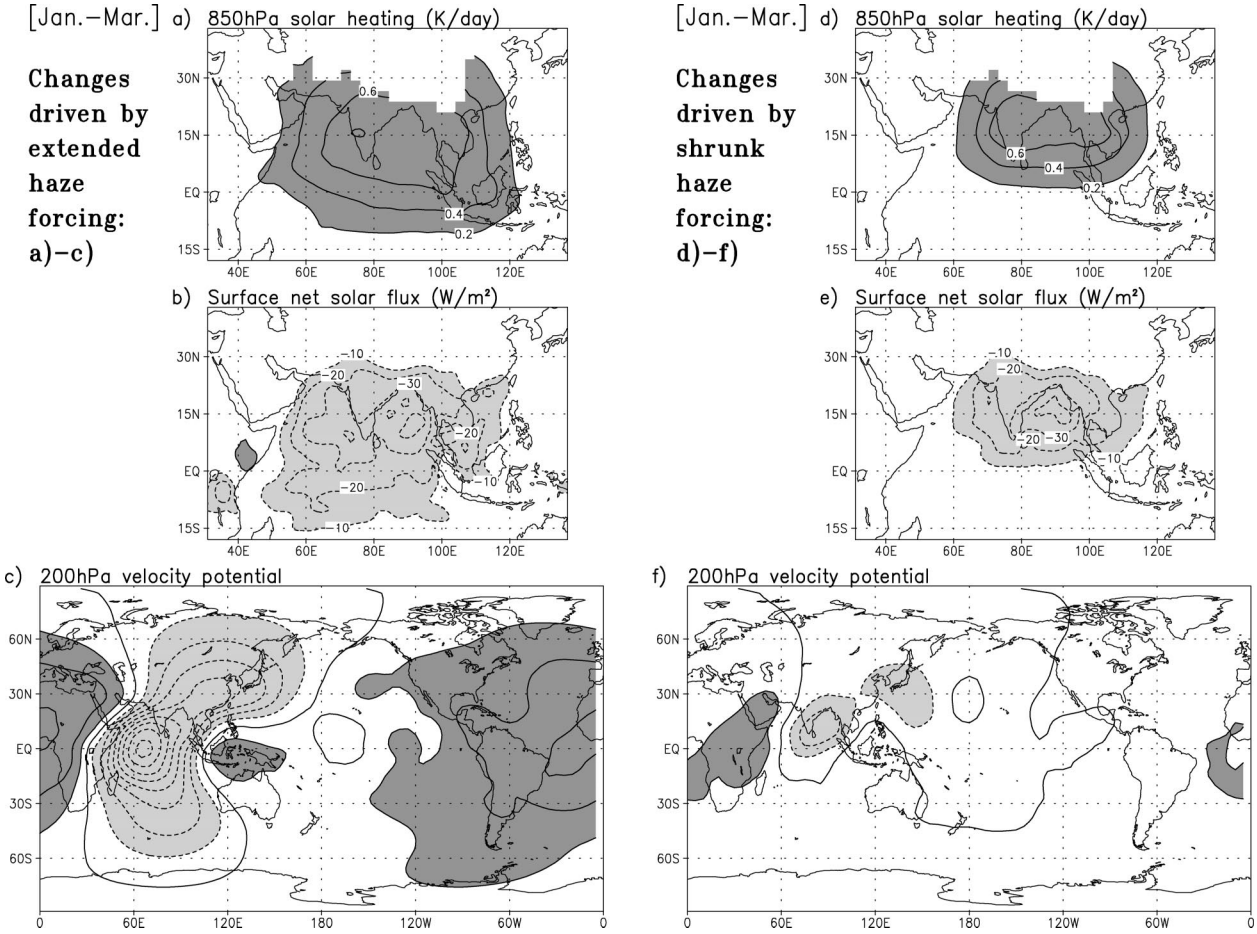

FIG. 3. Two CCM3 experiments of the SA haze effects using the NCAR CCM3: (a)–(c) the EHF experiment, and (d)–(f) the SHF experiment. All panels show the Jan − Mar difference between an experiment and the control run (no haze effect). The CCM3 was integrated with the climatological seasonal cycle of SSTs in all runs. In each experiment, the low-level atmospheric solar heating was increased and the net surface solar flux was reduced, as clear in (a), (b), (d), and (e); note that the imposed aerosol forcing is similar (but not identical) to what (a), (b), (d), and (e) depict, since the model's background radiation becomes slightly modified due to the forcing. In (c) and (f) the velocity potential from the wind change at 200 hPa is shown with the same contour interval in both. In these panels it is clear that the global effect of the SA haze depends *crucially* on the southern extent of the haze coverage. In all panels, positive (negative) values are shaded dark (light).

that the EHF forcing extends across the equator and its east–west spatial extent is also larger.

On the other hand, the local climate changes are very similar between the two haze forcings. Figure 4 demonstrates that the computed surface temperature changes for EHF and SHF within the domain of the haze forcing are strikingly similar, particularly over India where the forcing is centered. The local climate changes are similar, perhaps, because the changes are driven radiatively. Away from the forcing area, the surface temperature changes start to differ a lot more between the two simulations. Details of how the local climate responds to the haze are described in Chung et al. (2002). In the following, we mainly discuss the sensitivity of the climate change to the haze spatial extent, and the remote effects of the SA haze.

3. Wintertime southwest Asian drought

Southwest Asia is the region spanning from Syria and the Caucasus to Afghanistan and Pakistan. Southwest Asia has a wet season generally between November and April. Figure 5a shows the January–March precipitation change for the EHF experiment, and Fig. 5d shows the change for the SHF experiment. As discussed in section 2, most features in Fig. 5 are statistically significant at much higher than the 95% level in a standard *t* test. Both cases generate an enhancement of rainfall over the Indian peninsula and a rainfall suppression in SW Asia, with the EHF driving a more severe SW Asian drought.

The dynamical mechanisms by which the haze drives a drying over SW Asia in the model have been explained in Chung et al. (2002). Here we summarize their explanation with Fig. 5. As Figs. 5b and 5e show, the

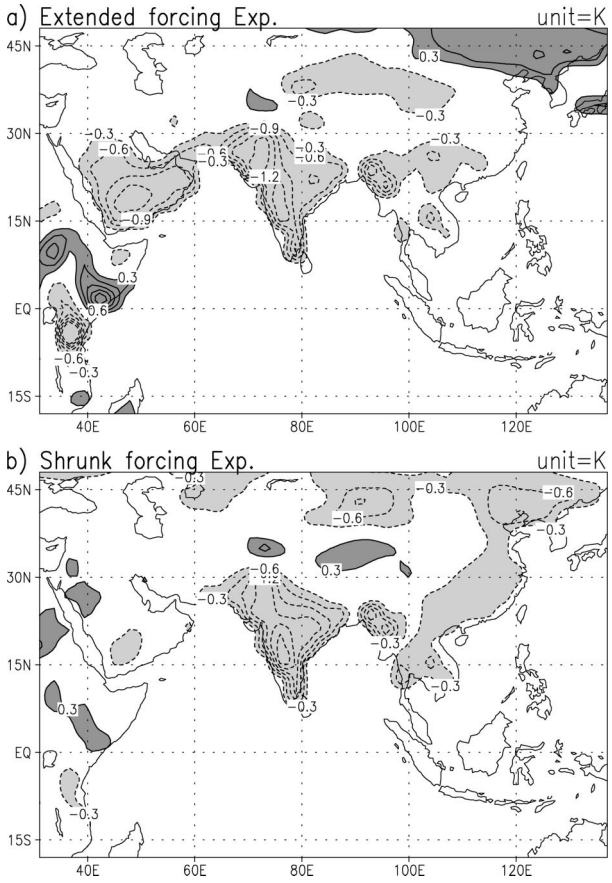

FIG. 4. Surface temperature change for the period Jan–Mar due to, (a) effect of the EHF and (b) effect of the SHF. Positive (negative) values are shaded dark (light).

aerosol forcing warms the low-level atmosphere over the northern Indian Ocean. The northward widening of the warm area enhances the convection over these areas. The linkage of the low-level aerosol heating to the convection enhancement aloft is shown in Figs. 5c and 5f, which show that the velocity potential of the 850-hPa wind change occurs in the same region as the warming of the low-level and the deep convection enhancement. The low-level convergence (positive contours in Figs. 5c and 5f) over the region with imposed aerosol forcing is accompanied by upper-level divergence (Figs. 3c and 3f). The increased convection (and thus increased rising motion) over tropical India and the Indian Ocean is balanced by the compensatory sinking motions over regions outside the haze region, such as over SW Asia and the western equatorial Pacific.

Is there observational evidence for the model prediction? It should first be pointed out that there is a large interannual variability (a few times the signal shown in Fig. 5) in the wintertime precipitation. The haze effect is just one of many factors regulating the precipitation. Nevertheless, the SW Asian region has been experiencing severe wintertime drought conditions in recent years (Barlow et al. 2002). In Barlow et al.'s study, the severe drought from 1998 until now is attributed to the anomalous La Niña (anomalous in the sense that the western Pacific warm waters extended far to the east). Although El Niño/La Niña events seem to exert a huge influence on the SW Asian precipitation, the current drought can also be a part of a long-term drying trend. As the haze release continues and the longer-term data become available, this issue can be clarified. The locations of the rainfall enhancements/suppressions differ somewhat from the observation counterpart (not shown; refer to Barlow et al.), but the overall pattern is quite similar to the haze effects as simulated by the CCM. Also, while the experiments show a sensitivity of the drought simulation to the haze forcing area, the haze distribution itself can be modulated by interannual variations in the atmospheric circulation (which in turn is influenced by El Niño/La Niña variability). Thus, the whole system is part of a complex feedback system between the spatial extent of the haze and the circulation.

4. Implication for ENSO characteristics

As discussed in section 1, the tropical Pacific surface has warmed in recent decades. The warming pattern is El Niño–like, that is, associated with a weakening of the zonal SST gradient (Meehl and Washington 1996). Recent studies have attempted to attribute this El Niño–like warming to a greenhouse warming. Meehl et al. (2000) summarized the coupled model responses to the CO_2 level increase. In their summary, the relative warming of the eastern Pacific was simulated only by some of the models, while other models showed the opposite response. Recently, Cai and Whetton (2001) proposed that the greenhouse gas–induced warming is initially La Niña–like and later becomes El Niño–like. The effects of greenhouse gases on the zonal SST gradient of the tropical Pacific seem very controversial at present. Clement et al. (1996) demonstrated that a uniformly increased heat forcing into the ocean leads to La Niña–like warming (i.e., a strengthened zonal SST gradient) because the vertical heat advection in the eastern basin becomes greater and cancels part of the warming forcing. Their calculation was later supported by an ocean GCM study (Seager and Murtugudde 1997). On the other hand, Meehl and Washington (1996) argued that the cloud feedback would act to reduce the zonal SST gradient in the tropical Pacific.

In this section, we will use the CCM3 to show that the SA haze can remotely suppress convection in the equatorial western Pacific. The convection suppression in the western Pacific leads to a weaker zonal gradient of deep diabatic heating over the tropical Pacific, and thus weaker trade winds. The weakening of the trade wind deepens the thermocline in the eastern basin and warms the overlying ocean. The weakened zonal gradient of SST further weakens the trade wind. As will

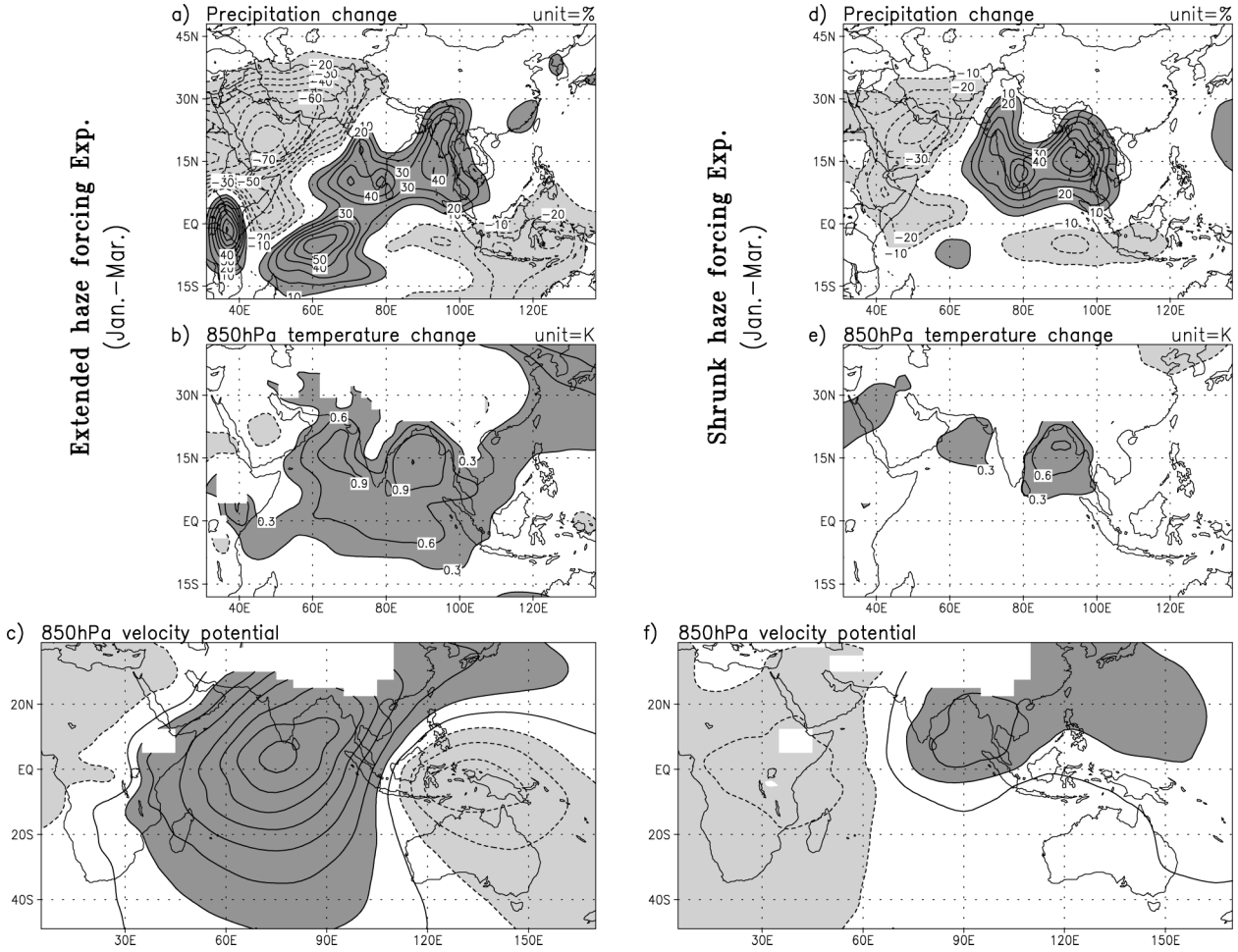

FIG. 5. Climate change for the period Jan–Mar due to, (a)–(c) effects of the EHF and (d)–(f) effects of the SHF. Panels (a) and (d) show the percentage precipitation change, and (b) and (e) display the 850-hPa temperature change. In (c) and (f) the velocity potentials from the 850-hPa wind changes are shown, using the same contour interval.

be shown, the western Pacific convection suppression depends crucially on the spatial extent of the haze. Furthermore, using the Cane–Zebiak coupled model (Zebiak and Cane 1987), we will show that the Pacific ocean–atmosphere coupled response to the haze-induced convection suppression is very similar to the observed El Niño–like warming for the EHF case.

a. CCM3 experiments and the Cane–Zebiak model

Figures 6a and 6b depict the wintertime (December–February) precipitation changes for the two CCM3 experiments. The focus is on the boreal winter season because the mature phase of ENSO event evolution occurs in this season. Both experiments show large perturbations far beyond the haze forcing area. These remote perturbations are found to be statistically significant relative to the CCM3 internal variability. The rainfall change in the SHF experiment is characterized by a northward migration toward the Bay of Bengal, while the EHF experiment additionally shows a westward shift toward the western Indian Ocean. Most of the precipitation change is due to changes in convective precipitation. The convection in the western equatorial Pacific is greatly suppressed in the EHF, apparently as a result of more extensive (i.e., over a larger area) enhanced convections over the Indian Ocean. The SHF simulation results in a much weaker suppression of convection in the western Pacific. Figure 6c shows changes in the deep diabatic heating (Q averaged from 400 hPa to 500 hPa), which resembles the precipitation changes shown in Fig. 6b. This similarity is not surprising since the latent heat component dominates the total diabatic heating in the Tropics. Our explanation for the simulated convection suppression in the western Pacific in the EHF experiment is based on the constraint that convergence in one region has to be balanced by divergence elsewhere (as indeed shown over Indonesia in Fig. 5c). As one Walker circulation cell encompasses the western Pacific (associated with the rising portion of the cell) and the Indian Ocean (sinking portion), the low-level convergence enhancement (thus precipitation enhancement) in the In-

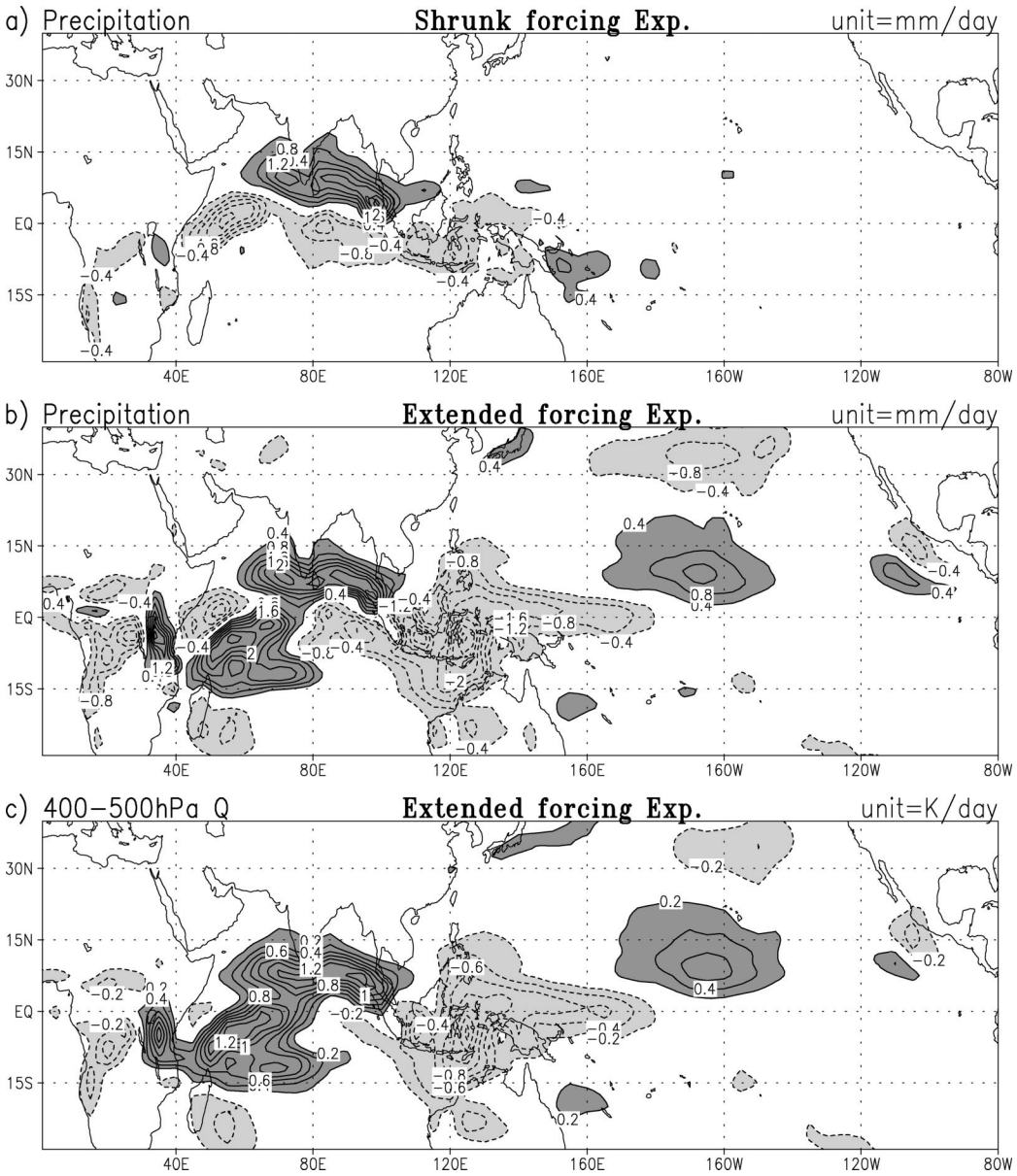

FIG. 6. Dec–Feb precipitation change with (a) the SHF experiment and (b) with the EHF. (c) Diabatic heating (Q) change averaged over the 400–500-hPa layer is displayed for the EHF experiment.

dian Ocean would weaken the low-level convection in the western Pacific.

Next we explore the impact of the convection suppression on the Pacific SST to see if the observed El Niño–like warming can be accurately simulated. For this quantitative assessment, another simulation was conducted with the Cane–Zebiak coupled anomaly model (Zebiak and Cane 1987). This model is a tropical Pacific domain model exclusively employing atmosphere/ocean dynamics of relevance to ENSO. The Cane–Zebiak (CZ) model mainly simulates interannual variability and has been extensively used for ENSO prediction. We expanded the deep heating domain of the model to include the Indian Ocean longitudes. Over this Indian–Pacific domain, the December–February mean CCM3 simulated deep heating anomalies (Fig. 6c) were added to the CZ model heating during December–February. The model was run with this heating anomaly for 1000 model years, and was contrasted with the run without the heating anomaly (see Fig. 7b). We followed Chung and Nigam's (1999) study, in inserting externally derived deep heating anomalies into the CZ atmosphere model.

Figure 7a shows the observed El Niño–like warming. In making this estimate, that is, via ENSO loading vector (see details in the next subsection), we minimized the contamination due to the decadal variability. Figure 7b

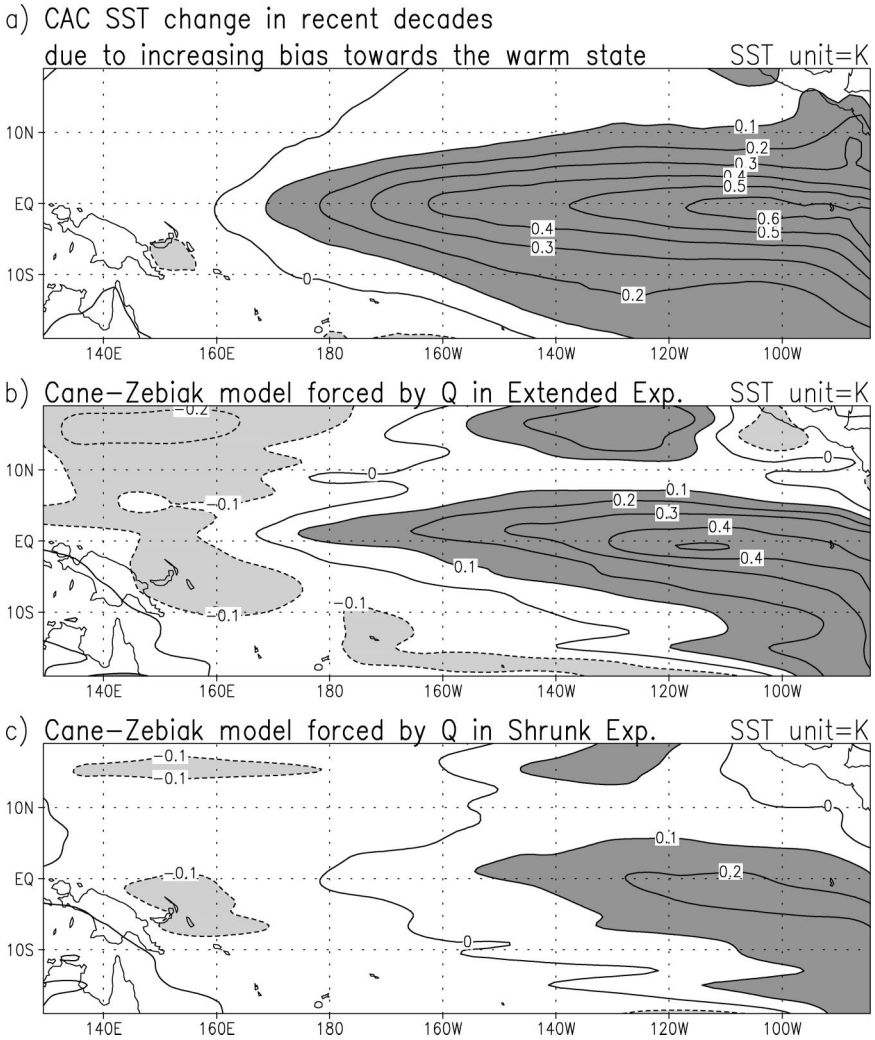

FIG. 7. Quantitative assessment of the linkage of the simulated precipitation change over the western equatorial Pacific (Fig. 6) to the observed El Niño–like warming in the tropical Pacific in the last three decades, using the Cane–Zebiak coupled model. (a) Estimate of the observed SST change up to ~2000 due to the increasing bias toward the El Niño (warm) phase, as obtained by multiplying the ENSO loading vector by 0.5 (details in the last paragraph of section 5b), (b) Cane–Zebiak coupled model response to Fig. 6c (400–500-hPa heating anomaly from the EHF experiment), and (c) CZ model response to 400–500-hPa *Q* anomaly from the SHF experiment. The coupled model was run for 1000 model years with this deep heating anomaly during Dec–Feb (experiment run) and without it (control run), and the annually averaged difference between the two runs is displayed in (b)–(c). The similarity between (a) and (b) indicates that the SA haze is a partial reason for the recent El Niño–like warming in the tropical Pacific.

shows the simulated change in SST by the CZ model. When Fig. 7a is compared with Fig. 7b, it is seen that the CZ model with the EHF diabatic heating anomaly simulates a warming in the central/eastern Pacific (Fig. 7b), and the warming amplitude is very close to that of the observed warming (Fig. 7a). Figure 7c depicts the CZ model response to the deep heating perturbation from the SHF experiment. The SHF also contributes to El Niño–like warming but only by slightly less than half of the observed magnitude. The results shown in Figs. 6 and 7 suggest that the SA haze may be partially responsible for the observed bias toward the warm state in the tropical Pacific.

b. ENSO time series

Here, we discuss ENSO time series using different indices in support of our hypothesis that the characteristics of the observed El Niño–like warming are more supportive of the haze than of the greenhouse gases for the underlying cause. The community standard for ENSO time series is presently the Niño-3.4 index, which

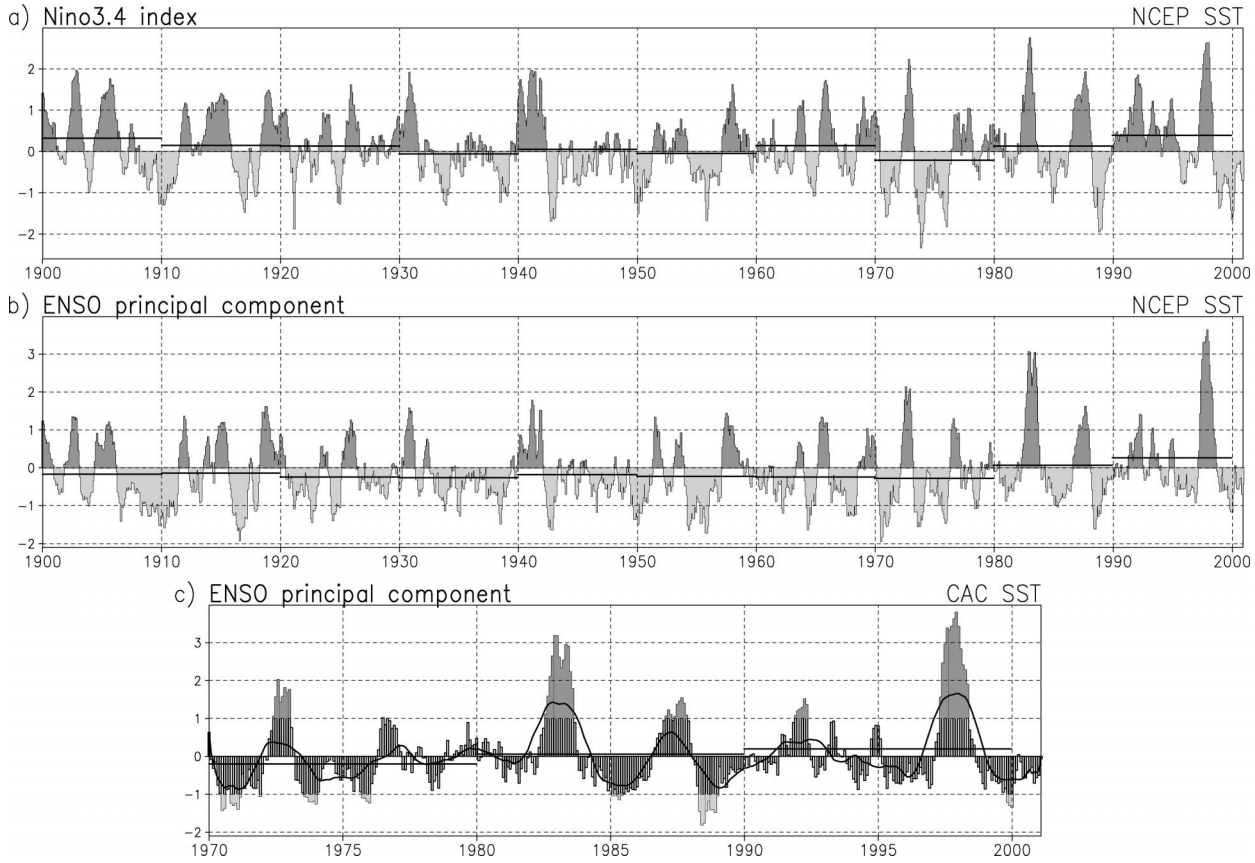

FIG. 8. ENSO time series: (a) NCEP SST anomaly over the Niño-3.4 region, (b) the principal component best corresponding to ENSO variability from RPCA of NCEP SST, and (c) the ENSO principal component from RPCA of CAC SST. The ENSO time series acquired from RPCA is much less contaminated by decadal fluctuation modes than the one from the Niño-3.4 index. The mean of the time series is shown for each decade using black horizontal line. In (c) the dark solid curve draws the moving averaged (2-yr band) principal component. The increasing bias toward the warm state is clearly demonstrated by the increasing decadal mean of ENSO principal components in the last 30 years or so.

is the SST anomaly averaged over the Niño-3.4 region (5°S–5°N, 170°–120°W). Quite a few studies used an EOF analysis or its variants to track the phase/amplitude of ENSO variability (e.g., Davey et al. 1994; Barnett 1991). If one is interested in extracting ENSO variability, it is important to filter out the Pacific decadal variability since ENSO and decadal variability have somewhat similar spatial patterns (Zhang et al. 1997). Nigam et al. (1999) demonstrated that a rotated principal component analysis (RPCA) well separates the decadal variability from the ENSO variability. In this subsection, we compare the Niño-3.4 index, to an RPCA-derived ENSO time series. When an RPCA is applied to the SST anomaly in the tropical Pacific, the leading mode always corresponds to ENSO variability. The principal component of the leading mode is referred to hereafter as ''ENSO principal component'' for brevity. The important period is the last three decades (1970–2000) when the SA haze concentration has presumably increased rapidly (see Krishnan and Ramanathan 2002).

In Fig. 8a, the Niño-3.4 index with the National Centers for Environmental Prediction (NCEP) SST is displayed for the period 1900–2000. The NCEP SST used in this study is a combination of Reynolds and Smith's (1994) SST for periods before November 1981 and the optimal interpolation (OI) SST (Kaplan et al. 1998) for the period from November 1981. The ENSO principal component for the 1900–2000 period as obtained with the NCEP SST is shown in Fig. 8b. In calculating this ENSO principal component, an RPCA was applied to the 1970–2000 SST anomaly relative to the 1970–2000 mean seasonal cycle over the 22.5°S–22.5°N, 127.5°E–72.5°W domain. The principal component obtained in this fashion only spans from 1970 to 2000. We then computed the 1900–69 anomaly with respect to the 1970–2000 mean seasonal cycle, and compared the anomaly with eight leading rotated loading vectors for an extension of the principal components. This comparison (using a least squares fit) led to an ENSO principal component that spans from 1900 to 2000 (Fig. 8b). The ENSO principal component in Fig. 8b is found to be very similar to the Niño-3.4 index on a 2–4-yr timescale, and somewhat different on longer (i.e., decadal) timescales perhaps due to much bigger effects of the

Pacific decadal variability on the Niño-3.4 index than on the ENSO principal component.

Our focus is on the decadal fluctuation of the ENSO time series. The black horizontal lines in Fig. 8 show the decadal means (i.e., arithmetic mean of the ENSO time series over each decade). According to the Niño-3.4 index, the 1980s and 1990s have warm biases, and so do a few other decades like the 1900s and 1910s. In contrast, the decadal mean of the ENSO principal component (Fig. 8b) remained almost unchanged until the 1970s, then increased from the 1970s to the 1980s, and again from the 1980s to the 1990s. To be sure that this finding with the ENSO principal component is not very data dependent, we analyzed the 1945–93 revised Comprehensive Ocean–Atmosphere Data Set (COADS; da Silva et al. 1994) and the 1970–2000 Climate Analysis Center (CAC) SST. ENSO principal components behave similarly with these datasets. The fact that the decadal mean has remained about the same until the 1970s (Fig. 8b) is supportive of a causal factor other than the greenhouse gas increase. According to our hypothesis, the SA haze would amplify El Niño events and weaken La Niña events, very similar to the observations shown in Fig. 8b.

The warming trend of the ENSO principal component from the 1970s to the 1990s is further shown using the $2^\circ \times 2^\circ$ resolution CAC SST (spanning 29°S–29°N, 124°E–70°W) in Fig. 8c. This figure also shows a 2-yr moving average (see the solid line). During the 1970s, El Niño was as strong as La Niña. During the 1990s, El Niño amplitudes were much stronger than those of La Niña. If the ENSO time series is redefined as the departure from its decadal mean, then El Niño/La Niña amplitude ratio would not seem very different from one decade to another. The change in the decadal-mean ENSO principal component (Fig. 8c) up to the year 2000 is about $+0.5$ (from -0.25 to 0.25). The leading loading vector (corresponding to the ENSO principal component) in the RPCA of CAC SST was multiplied by 0.5 in order to estimate the tropical Pacific temperature change due to the increased bias toward the warm phase (Fig. 7a).

5. Implication for AO

The main characteristic of the AO is a meridional fluctuation of the zonal-mean zonal momentum on timescales from days to decades. Figure 9a shows the structure of the AO covariant zonal-mean zonal wind in the 1949–2000 NCEP–NCAR reanalyses.[1] Thompson et al. (2000) analyzed the recent behavior of the AO and concluded that the AO has preferred its positive phase (i.e., the poleward shift of zonal momentum) and this upward trend of the AO is most significant from January to March. Figure 9b depicts the January–March zonal-mean zonal wind change from 1970 to 2000 in the NCEP reanalyses, using a linear trend analysis. The striking similarity between Figs. 9a and Fig. 9b reveals that the upward trend in the AO explains a significant portion of the recent NH climate trend, as previously demonstrated by DeWeaver and Nigam (2000). Another important, and more recent, finding of the recent AO characteristics is an increasing variance of the AO index (Feldstein 2002). In what follows, we propose that the fluctuating SA haze forcing can partly explain the increasing variance of the AO index. In this study, we do not distinguish between NAO, AO, and NH annular mode, following Wallace's (2000) suggestion.

Figure 9c shows the CCM3 AO, which was extracted from the CCM3 control run (CCM3 plus climatological seasonal cycle of SST, and without haze effects). The CCM3 AO (Fig. 9c) is somewhat different from the NCEP AO (Fig. 9a), but the deficiency (notably northward shift of the overall pattern) does not seem significant for our purpose. In plotting Figs. 9a–c, we first calculated the AO principal component, from an RPCA on combined variables of 200-hPa height (HGT), 850-hPa temperature (T), and 500–200-hPa diabatic heating (Q) anomalies. Then zonal mean zonal winds at all levels were regressed against the AO principal component to obtain the AO covariant zonal mean zonal wind (Figs. 9a–c). The choice of the three variables in the combined RPCA was to give the same weight to the Tropics and the extratropics; the diabatic heating anomaly is largest in the Tropics while height and temperature vary more in the extratropical region.

First, we describe the effects of the SA haze on the NH zonal mean zonal wind during January–March. Figure 9d shows the effects of the EHF, and Fig. 9e shows the effects of the SHF. As evident from the figure, the EHF effectively pushes the westerly zonal momentum poleward, while the SHF reveals a much weaker (thus statistically somewhat insignificant) response. Such a large sensitivity of the zonal mean zonal wind to the southern extent of the SA haze forcing area can be one explanation for Feldstein's (2002) finding that the variance of the observed AO index has increased recently. Analysis of the probability distribution function (PDF) of the AO index (not shown) strengthens the connection of the SA haze with the increasing variance.

Second, we seek to understand the significance of the EHF effects on the zonal-mean zonal wind. Quantitatively, the zonal-mean wind change driven by the EHF can explain about half of the observed zonal-mean wind trend (change from 1970 to 1999 as estimated by a linear trend analysis; Fig. 9b), whereas the NCEP AO (Fig. 9a) is of the same magnitude as the CCM3 AO (Fig. 9c). Figure 9d, when compared with Fig. 9c, shows that the EHF can generate about two-thirds of the observed AO upward trend. When variables other than the zonal-mean zonal wind are analyzed, it appears that the SHF and the EHF both exert a significant influence. For ex-

[1] The choice of the period 1949–2000 is to make full use of the available NCEP–NCAR reanalyses so that the AO structure can be more accurately extracted.

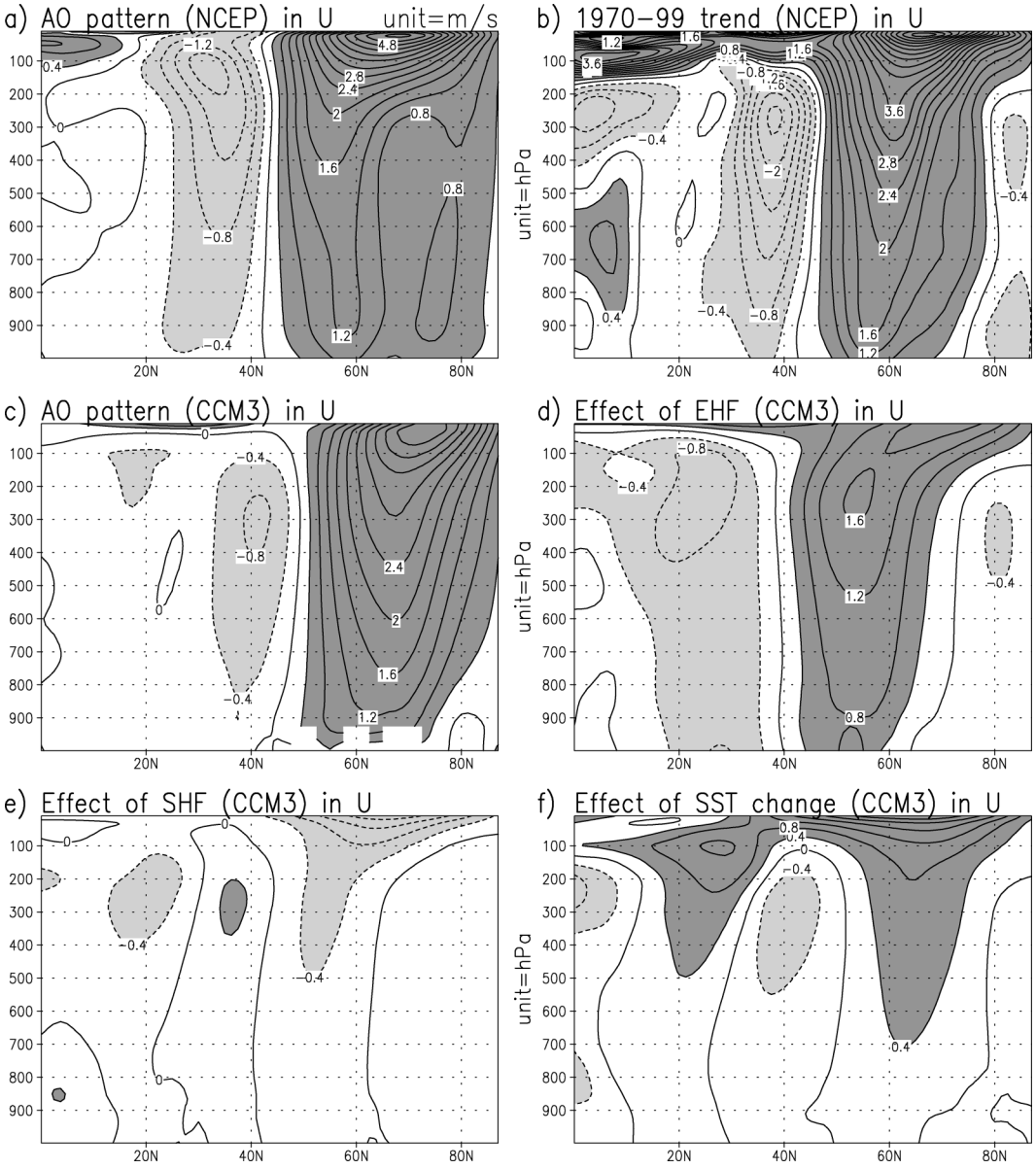

FIG. 9. Zonal-mean zonal wind (unit = m s^{-1}): (a) AO covariant component in 1949–2000 NCEP reanalyses, (b) linear trend in 1970–99 NCEP reanalyses, (c) AO covariant component in 85 yr of CCM3 control run (CCM3 plus SST climatology), (d) effect of the EHF, (e) effect of the SHF, and (f) effect of the SST changes from 1970 to 2000 SST in the CCM3. All the panels show the average for the period Jan–Mar; shading and contouring as in Fig. 3.

ample, the NH extratropical surface temperature is considerably perturbed in both the SHF and the EHF experiments (not shown). The actual temperature change patterns are very different between the two experiments; while both the EHF and SHF simulations generate warm anomalies in Canada, the EHF simulates warm anomalies in northeast Asia and the SHF case leads to cold anomalies in that region. The overall structure of perturbation in wind, height, temperature, etc., associated with the EHF projects well onto the AO pattern. However, the large-scale NH mean climate change driven by the SHF bears very little resemblance to the AO.

It has been suggested (e.g., Rodwell et al. 1999) that the change in the observed SST during the last few decades can possibly force the upward trend in the AO. We examined this possibility (Fig. 9f) by conducting a CCM3 simulation with a modified SST that mimics the observed change in SST between 1970 and 2000. We estimated (using a linear trend analysis) the observed change for each grid in the monthly mean SST and added this change to the seasonally varying SST climatology used in the CCM3. The resulting changes in the zonal mean wind are shown in Fig. 9f. The amplitude of the change in the zonal mean wind is much weaker

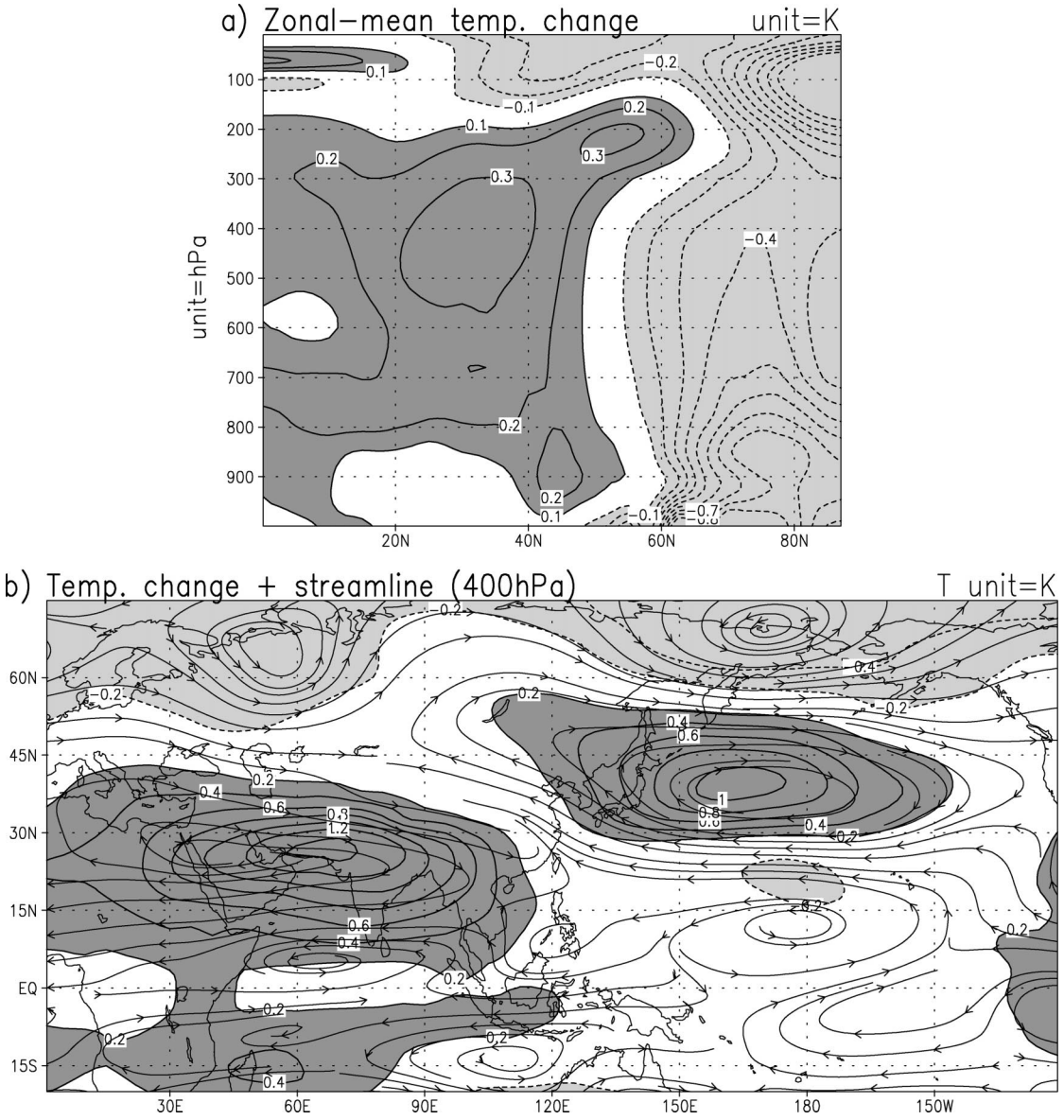

FIG. 10. Effects of the EHF on Jan–Mar temperature and wind: (a) zonal mean temperature and (b) temperature and streamline at the 400-hPa level.

than those shown in Fig. 9b and the latitudinal pattern is also remarkably different. In summary, Fig. 9f shows that the SST boundary condition change is much less effective in impacting the extratropical zonal-mean zonal wind when compared with the EHF effect (at least in the context of the CCM3).

The large impact of the SA haze forcing (particularly the EHF) on the hemispheric circulation is not too surprising, in view of the diagnostic study by Branstator (1985) which revealed South Asia to be a very effective area for stimulating flow changes in the extratropics. We next illustrate the mechanism by which the EHF leads to a poleward movement of the zonal momentum. Our proposed mechanism is based upon the thermal wind relationship that relates meridional temperature gradient to vertical wind shear. The January–March climatology of the zonal mean U has a maximum at 30°N around 200 hPa and at 45°N near the surface. Thus, a temperature increase along 30°–40°N would act to increase the zonal mean U north of the 30°–40°N zone and decrease U south of the zone (from thermal wind relation). The zonal mean T change due to the haze is shown in Fig. 10a. In this figure, the temperature increase is maximized around 30°N at the 400-hPa level and around 40°N in the lower troposphere. This 3D temperature change structure, from the thermal wind relation, would force the AO to prefer its high index phase (i.e., northward shift of the jet stream). One might

call this explanation into question, though, by suggesting an alternate possibility that most of the simulated zonal mean *T* change in Fig. 10a was simply due to a tropospheric adjustment of the *T* field to the changes in *U* forced by a positive AO phase (Fig. 9c). We ruled out this possibility because the CCM3 AO covariant zonal mean *T* (not shown) resembles the temperature change driven by the EHF effects only in the high latitudes. Therefore, we infer that most of the computed change in the zonal mean *T* (Fig. 10a) is due to the direct effects of the EHF.

This inference is also supported by an examination of the regional temperature pattern. Figure 10b displays the temperature changes at 400 hPa, along with the changes in wind denoted by streamlines. At the 850-hPa level (not shown), the warming over northeastern China, Korea, and Japan is responsible for most of the zonal mean *T* increase at 40°N, while at 400 hPa (Fig. 10b) two broad warming regimes, one centered over Afghanistan and the other east of Japan/Korea, contribute to most of the zonal mean warming shown in Fig. 10a. Most of these major warming features result mainly from the regional circulation changes. The warming centered over Afghanistan is driven by an enhanced sinking motion that adiabatically heats the atmosphere. The warming around Japan is, on the other hand, driven by horizontal temperature advections. Streamlines are superimposed in Fig. 10b to illustrate the flow anomalies associated with anomalous temperature advections. At the 850-hPa level, the wind change (as inferable from Fig. 5c) is essentially cyclonic around the haze forcing area, which explains the SW flow over East Asia. The cyclonic feature arises from an enhanced convection over the northern Indian Ocean (Fig. 6b). Climatologically, the atmosphere over Japan has a very sharp meridional gradient during boreal winter, and as a result even a mild SW flow anomaly can increase the temperature substantially. An important implication is that the longitudinal location of the haze and, by this, of the diabatic heating, plays an important role in perturbing the extratropical climate. This finding is not inconsistent with Branstator's (1985) results.

6. Discussion and conclusions

The South Asian (SA) haze is widespread over the northern Indian Ocean and the south Asian continent during the dry season (November–April). In addition, since the aerosol distribution is controlled by transport that in turn varies interannually, the aerosol radiative forcing varies in magnitude, spatial extent, and vertical structure from year to year. This paper has shown that fluctuations in the absorbing aerosol forcing can play a major role in interannual climate variability in the Tropics and the extratropics. Using the CCM3, we have first shown that the climate is sensitive to the southern extent of the SA haze forcing but mainly outside the forcing area. Focusing on the remote effects of the haze, we showed that some of the recent observed NH wintertime changes of the SW Asian monsoon, ENSO, and the AO could be explained by the SA haze forcing and its fluctuation. The two forcing patterns used to illustrate our results differ essentially in their southward extent, with the extended haze forcing (EHF) extending across the equator while the shrunk haze forcing (SHF) is restricted to the regions north of the equator. We treated these two as stationary patterns and conducted multiyear simulations. In reality, however, the spatial extent varies from year to year (and even month to month), and thus our results only hint at (as opposed to demonstrating) potentially large contributions of the haze to some of the recent observations with regards to the drought in SW Asia and the phase changes in ENSO and AO. Other factors, such as interannual variations of SSTs, would also play some role. Given the primitive knowledge of the variability of the haze forcing, it is premature to attempt a more sophisticated simulation of the haze variations at this time.

Nevertheless it is our hope that this study will stimulate climate diagnosticians to explore these issues in more detail. In fact, we revisited the ENSO time series issue in this paper (see section 4b) to explore the role of the absorbing haze. An RPCA of the SST anomaly in the tropical Pacific yielded an ENSO time series (Fig. 8), the decadal mean of which remained constant till the 1970s, and then increased from the 1970s to the 1980s and again from the 1980s to the 1990s. This behavior of an RPCA-based ENSO time series by itself is suggestive of a non-greenhouse-gas anthropogenic source for its origin, since the greenhouse gas increase began in the late nineteenth century. For this reason as well, we are raising the SA haze as a possible explanation for the observed El Niño–like warming. The trends in South Asian SO_2 emissions (source of sulfates in the haze) suggest that the most dramatic increase in the haze must have begun after 1970 (Krishnan and Ramanathan 2002).

One difficulty in finding convincing observational support for the present results is the presence of large interannual variability that obscures any long-term trend. For example, our proposed mechanism for El Niño–like warming relies crucially on the suppressed convection in the tropical western Pacific. If the proposed mechanism has indeed played a role, there should have been a trend of suppression of convection in the western Pacific. Regarding the SW Asian winter monsoon, Barlow et al. (2002) identified the drought over this area in recent years as unprecedented. If the haze has driven a drying over SW Asia, there should have been a long-term decreasing precipitation trend in this area as well. On the other hand, the trends suggested by our results are much weaker than the interannual variability, thereby making it very hard to extract the relevant signals. In other words, the trend itself arises from a slight shift in the probability distribution function (PDF) of the precipitation, as shown in Fig. 11. Figure

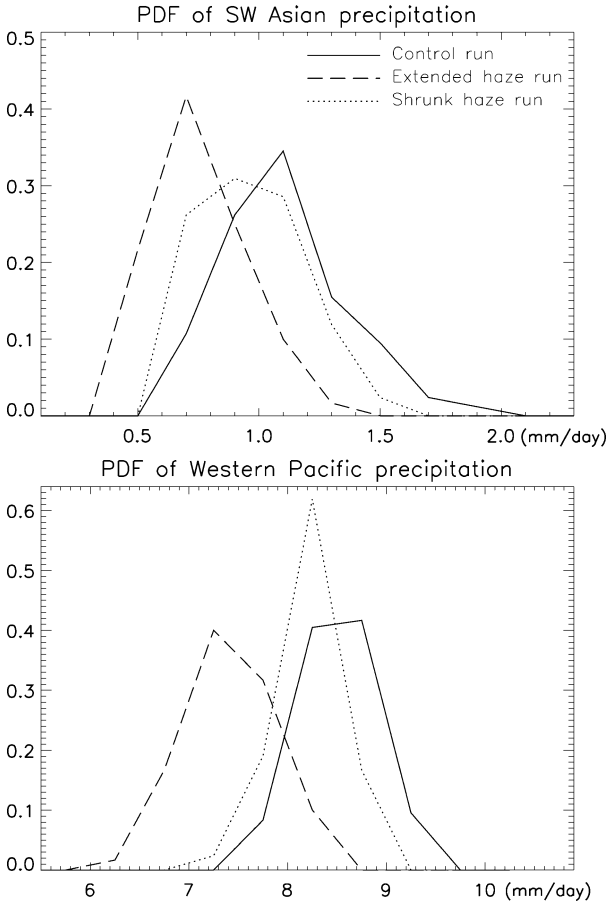

FIG. 11. The PDF of the precipitation (mm day^{-1}) for (a) SW Asia (25°–40°N, 50°–65°E) and (b) the equatorial western Pacific (10°S–10°N, 110°–150°E). In the PDF calculation, the Jan–Mar mean model outputs were used; long dash lines denote results from the EHF run and dot lines denote those from the SHF run.

11 (top) shows the PDF of January–March SW Asian precipitation for each of the three runs, and (bottom) the PDF of the tropical western Pacific precipitation during the same period. All the lines corresponding to the experiments in Fig. 11 are significantly different (in a statistical sense) from that of the control run when the standard K–S test (Kolmogorov–Smirnov test; Chakravarti et al. 1967, 392–394) is applied. In both the panels, the SA haze forcing shifts the PDF shape only slightly, leaving a significant portion of overlap. This means that both the hazy climate and the nonhazy climate would have wet months and dry months occur often, while the haze would cause dry weather to occur relatively more frequently (or longer) in SW Asia.

With respect to the role of the aerosol in warming the tropical Pacific, there is one more complication. Even if there had indeed been a decreasing convection it could have resulted simply from the increasing bias toward the warm state (i.e., El Niño–like warming). The real question is whether the convection in the western Pacific has decreased more than it would have due only to the warming trend of ENSO time series. We conducted a preliminary analysis of the linear trend in the 1975–2000 outgoing longwave radiation (OLR) with two approaches. In one approach, unprocessed OLR was analyzed for the trend during January–March (not shown). In the other approach, the component of OLR that is covariant with the tropical SST anomaly was removed and then analyzed for the trend (again not shown). These analyses support our hypothesis by and large, but the detailed pattern and magnitude of the OLR trend is not very consistent with our simulated convection suppression. Similarly, in support of our proposal for the upward trend of the AO, we found some warming trend features over SW Asia and East Asia in the NCEP reanalyses (not shown), but there are discrepancies regarding the detailed pattern and magnitude. Much work is to be done in this regard. In particular, we have to allow the global ocean to respond to the aerosol forcing and account for the interannual variations in the 3D atmospheric haze forcing.

Another implication of our investigation is that the upward trend of the AO, as well as El Niño–like warming, contributes to the global warming. Strengthening of the extratropical westerlies brings more warm maritime air over land and more cold continental air over the ocean during wintertime. However the whole area mean is subject to a temperature increase because the lower-heat-capacity land surface areas undergo larger temperature changes than the oceanic surface. Wallace et al. (1995) demonstrated that the cold ocean–warm land (COWL) pattern is closely linked to hemispheric mean surface temperature anomaly. This sort of circulation-driven temperature change seems to explain a substantial portion of the recent global warming. The global mean of the observed surface temperature (Jones et al. 2001) shows a warming trend with the trend being conspicuous owing to the rapid warming during the 1980s and the 1990s. The 1990s was the warmest decade during the twentieth century. The recent warming has been largest over the land in midlatitudes and during winter and spring, associated with some cooling over the northern oceans, as the AO has a preferred positive phase (Hurrell 1996). Therefore, the remote impact of the extended SA haze on the ENSO and AO points to the possibility that aerosols are a surface warming source for regions outside the haze.

Acknowledgments. We thank Dr. F. Li of Scripps Institution for providing AOD data in generating Fig. 1. Also, we would like to thank Dr. S. Nigam of the University of Maryland and Dr. E. DeWeaver of the University of Wisconsin for various discussions of AO. This work was funded by a NSF Grant (ATM-0201946) and Vetlesen Foundation support to the Scripps Institution of Oceanography.

REFERENCES

Barlow, M., H. Cullen, and B. Lyon, 2002: Drought in central and southwest Asia: La Niña, the warm pool, and Indian Ocean precipitation. *J. Climate,* **15,** 697–700.

Barnett, T. P., 1991: The interaction of multiple time scales in the tropical climate system. *J. Climate,* **4,** 269–285.

Branstator, G., 1985: Analysis of general circulation model sea-surface temperature anomaly simulations using a linear model. Part I: Forced solutions. *J. Atmos. Sci.,* **42,** 2225–2241.

Cai, W., and P. H. Whetton, 2001: A time-varying greenhouse warming pattern and the tropical–extratropical circulation linkage in the Pacific Ocean. *J. Climate,* **14,** 3337–3355.

Chakravarti, I. M., G. R. Laha, and J. Roy, 1967: *Handbook of Methods of Applied Statistics.* Vol. I. John Wiley and Sons, 460 pp.

Chung, C. E., and S. Nigam, 1999: Asian summer monsoon—ENSO feedback on the Cane–Zebiak model ENSO. *J. Climate,* **12,** 2787–2807.

——, V. Ramanathan, and J. T. Kiehl, 2002: Effects of the south Asian absorbing haze on the northeast monsoon and surface–air heat exchange. *J. Climate,* **15,** 2462–2476.

Clement, A. C., R. Seager, M. A. Cane, and S. E. Zebiak, 1996: An ocean dynamical thermostat. *J. Climate,* **9,** 2190–2196.

da Silva, A. M., C. C. Young, and S. Levitus, 1994: *Algorithms and Procedures.* Vol. 1, *Atlas of Surface Marine Data 1994,* NOAA Atlas NESDIS 6, 83 pp.

Davey, M. K., S. Ineson, and M. A. Balmaseda, 1994: Simulation and hindcasts of tropical Pacific Ocean interannual variability. *Tellus,* **46A,** 433–447.

DeWeaver, E., and S. Nigam, 2000: Do stationary waves drive zonal-mean jet anomalies of the northern winter? *J. Climate,* **13,** 2160–2176.

Feldstein, S. B., 2002: The recent trend and variance increase of the annular mode. *J. Climate,* **15,** 88–94.

Gillett, N. P., M. R. Allen, R. E. McDonald, C. A. Senior, D. T. Shindell, and G. A. Schmidt, 2002: How linear is the Arctic Oscillation response to greenhouse gases? *J. Geophys. Res.,* **107** (D3), 4022, doi:10.1029/2001JD000589.

Hartmann, D. L., J. M. Wallace, V. Limpasuvan, D. W. J. Thompson, and J. R. Holton, 2000: Can ozone depletion and global warming interact to produce rapid climate change? *Proc. Natl. Acad. Sci. USA,* **97,** 1412–1417.

Hurrell, J. W., 1996: Influence of variations in extratropical wintertime teleconnections on Northern Hemisphere temperature. *Geophys. Res. Lett.,* **23,** 665–668.

James, P. M., and I. N. James, 1992: Spatial structure of ultra-low frequency variability of the flow in a simple atmospheric circulation model. *Quart. J. Roy. Meteor. Soc.,* **118,** 1211–1233.

Jones, P. D., T. J. Osborn, K. R. Briffa, C. K. Folland, E. B. Horton, L. V. Alexander, D. E. Parker, and N. A. Rayner, 2001: Adjusting for sampling density in grid box land and ocean surface temperature time series. *J. Geophys. Res.,* **106,** 3371–3380.

Kaplan, A., M. Cane, Y. Kushnir, A. Clement, M. Blumenthal, and B. Rajagopalan, 1998: Analyses of global sea surface temperature 1856–1991. *J. Geophys. Res.,* **103,** 18 567–18 589.

Kiehl, J. T., J. J. Hack, G. B. Bonan, B. A. Boville, D. L. Williamson, and P. J. Rasch, 1998: The National Center for Atmospheric Research Community Climate Model: CCM3. *J. Climate,* **11,** 1131–1149.

Krishnan, R., and V. Ramanathan, 2002: Evidence of surface cooling from absorbing aerosols. *Geophys. Res. Lett.,* **29** (9), 1340, doi: 10.1029/2002GL014687.

Li, F., and V. Ramanathan, 2002: Winter to summer monsoon variation of aerosol optical depth over the tropical Indian Ocean. *J. Geophys. Res.,* **107** (D6), 4284, doi:10.1029/2001JD000949.

Meehl, G. A., and W. M. Washington, 1996: El Niño–like climate change in a model with increased atmospheric CO_2 concentrations. *Nature,* **382,** 56–60.

——, G. J. Boer, C. Covey, M. Latif, and R. J. Stouffer, 2000: The Coupled Model Intercomparison Project (CMIP). *Bull. Amer. Meteor. Soc.,* **81,** 313–318.

Nigam, S., M. Barlow, and E. H. Berbery, 1999: Pacific decadal SST variability: Effects on U.S. drought and streamflow. *Eos, Trans. Amer. Geophys. Union,* **80,** 621–625.

——, C. Chung, and E. DeWeaver, 2000: ENSO diabatic heating in ECMWF and NCEP–NCAR reanalyses, and NCAR CCM3 simulation. *J. Climate,* **13,** 3152–3171.

Podgorny, I. A., and V. Ramanathan, 2001: A modeling study of the direct effect of aerosols over the tropical Indian Ocean. *J. Geophys. Res.,* **106,** 24 097–24 105.

Ramanathan, V., and Coauthors, 2001: Indian Ocean Experiment: An integrated analysis of the climate forcing and effects of the great Indo-Asian haze. *J. Geophys. Res.,* **106,** 28 369–28 370.

Reynolds, R. W., and T. M. Smith, 1994: Improved global sea surface temperature analyses using optimum interpolation. *J. Climate,* **7,** 929–948.

Robock, A., and J. Mao, 1992: Winter warming from large volcanic eruptions. *Geophys. Res. Lett.,* **19,** 2405–2408.

Rodwell, M. J., D. P. Rowell, and K. C. Folland, 1999: Oceanic forcing of the wintertime North Atlantic oscillation and European climate. *Nature,* **398,** 320–323.

Seager, R., and R. Murtugudde, 1997: Ocean dynamics, thermocline adjustment, and regulation of tropical SST. *J. Climate,* **10,** 521–534.

Thompson, D. W. J., and J. M. Wallace, 2000: Annular modes in the extratropical circulation. Part I: Month-to-month variability. *J. Climate,* **13,** 1000–1016.

——, ——, and G. C. Hegerl, 2000: Annular modes in the extratropical circulation Part II: Trends. *J. Climate,* **13,** 1018–1036.

Trenberth, K. E., and T. J. Hoar, 1996: The 1990–1995 El Niño–Southern Oscillation event: Longest on record. *Geophys. Res. Lett.,* **23,** 57–60.

——, and ——, 1997: El Niño and climate change. *Geophys. Res. Lett.,* **24,** 3057–3060.

Wallace, J. M., 2000: North Atlantic Oscillation/Annular Mode: Two paradigms—One phenomenon. *Quart. J. Roy. Meteor. Soc.,* **126,** 791–805.

——, Y. Zhang, and J. A. Renwick, 1995: Dynamic contribution of hemispheric mean temperature trends. *Science,* **270,** 780–783.

Xie, P., and P. A. Arkin, 1997: Global precipitation: A 17-year monthly analysis based on gauge observations, satellite estimates, and numerical model outputs. *Bull. Amer. Meteor. Soc.,* **78,** 2539–2558.

Zebiak, S. E., and M. A. Cane, 1987: A model El Niño–Southern Oscillation. *Mon. Wea. Rev.,* **115,** 2262–2278.

Zhang, Y., J. M. Wallace, and D. S. Battisti, 1997: ENSO-like interdecadal variability: 1900–93. *J. Climate,* **10,** 1004–1020.